Graphene Nanoribbons as Low Band Gap Donor Materials for Organic Photovoltaics: Quantum Chemical Aided Design

Silvio Osella,[†,*] Akimitsu Narita,[§] Matthias Georg Schwab,[‡] Yenny Hernandez,[§] Xinliang Feng,[§] Klaus Müllen,[§] and David Beljonne[†,*]

[†]Chemistry of Novel Materials, University of Mons, Place du Parc 20, B-7000 Mons, Belgium, [‡]BASF SE, Carl-Bosch-Strasse 38, 67056 Ludwigshafen, Germany, and [§]Max Planck Institute for Polymer Research, Ackermannweg 10, D-55128 Mainz, Germany

ABSTRACT

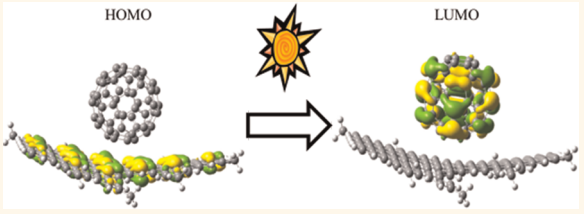

Graphene nanoribbons (GNRs) are strips of graphene cut along a specific direction that feature peculiar electronic and optical properties owing to lateral confinement effects. We show here by means of (time-dependent) density functional theory calculations that GNRs with properly designed edge structures fulfill the requirements in terms of electronic level alignment with common acceptors (namely, C_{60}), solar light harvesting, and singlet−triplet exchange energy to be used as low band gap semiconductors for organic photovoltaics.

KEYWORDS: graphene nanoribbon · band gap · organic photovoltaic · density functional theory

Graphene, a single layer of graphite,[1] has been extensively studied worldwide since the discovery of its remarkable electronic properties.[2−6] When graphene is cut along a specific direction, a strip of graphene with a nanometer sized width (<10 nm) is obtained, which is referred to as a graphene nanoribbon (GNR). Compared to graphene, GNRs show distinctive features in their electronic structure and optical properties, such as the opening of a finite band gap (graphene being a zero-overlap semimetal), which makes them attractive materials for carbon-based nanoelectronics.[7−10]

The geometrical arrangement of carbon atoms at the periphery, the passivation of the end carbon atoms with, for example, hydrogens, and the finite width of the GNRs strongly affect their electronic properties.[11−14] These confinement effects yield an increased band gap in armchair edge nanoribbons (A-NRs) that behave as semiconductors. A-NRs feature band gaps that scale inversely proportional to the ribbon width[11,15−19] and are highly sensitive to the number of armchair chains across the ribbon.[20−22] GNRs delineated with zigzag edges (Z-NRs) are typically metallic because of the spin-ordered states at the edges,[7,15,23−25] with those states localized near the Fermi level; nanoribbons with a higher fraction of zigzag edges exhibit a smaller band gap than a predominantly armchair edge ribbon of similar width.[20] Those peculiarities have raised the interest of scientists for the design, synthesis, and electrical characterization of GNRs.

Finite widths combined with periphery effects also provide GNRs with peculiar optical properties.[26,27] In particular, the absorption spectra of A-NRs exhibit strong anisotropy for the polarization direction of the incident light:[28] a number of absorption peaks appear when the polarization is parallel to the longitudinal length of the ribbon (resulting from direct interband transitions), while only one band is present when the polarization is set perpendicular to the ribbon (associated with an indirect interband transition).[29,30] On the other hand, Z-NRs show a different behavior with respect to polarization of light: the direct interband transition is forbidden for light polarized along the NR length but is allowed when the light polarization is perpendicular to the ribbon.[30] Another important feature pertaining to graphene ribbons is the existence of edge states, which play an important role in the optical absorption spectrum in the visible range.[26]

* Address correspondence to silvio.osella@umons.ac.be, david.beljonne@umons.ac.be.

Received for review April 4, 2012 and accepted May 25, 2012.

Published online May 25, 2012
10.1021/nn301478c

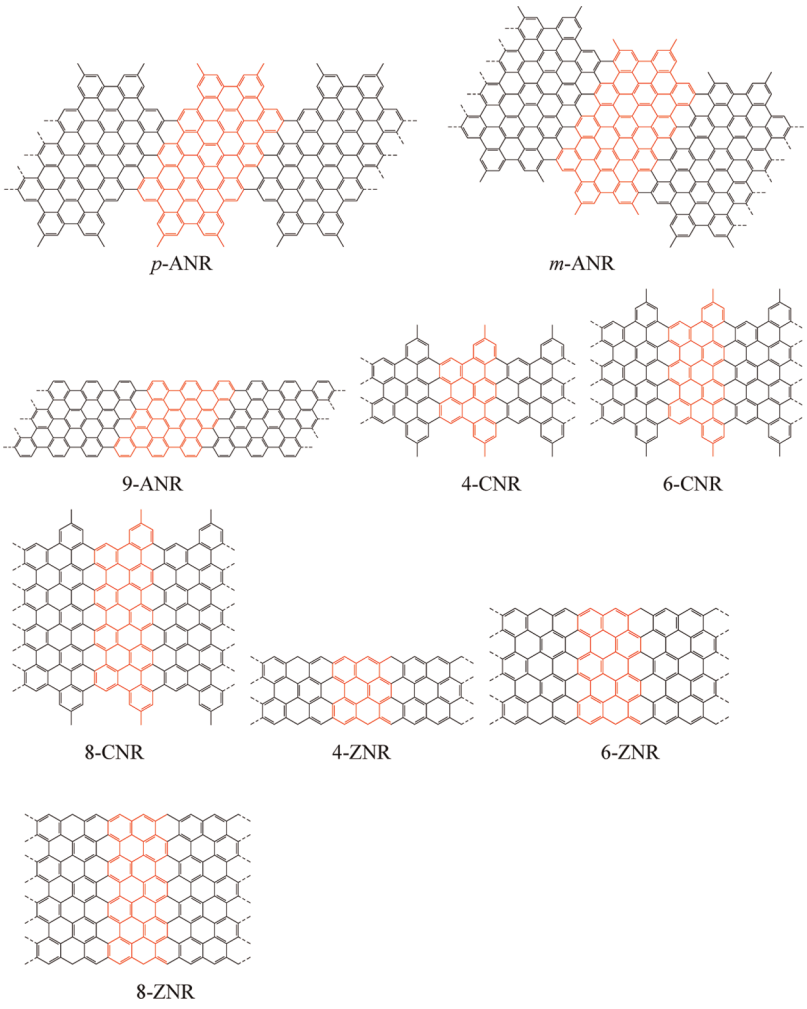

Figure 1. Chemical structures of the GNRs investigated here. The central red parts highlight the monomers; the dashed lines at the edges indicate the direction of elongation of the ribbons. *p*-ANR and *m*-ANR have the same repeating unit but differ by their connectivity. The difference in the CNR series is due to the increase of the width in the sequence 4-CNR < 6-CNR < 8-CNR. 9-ANR and [4,6,8]-ZNR are model structures for armchair and zigzag ribbons, respectively. For all structures, methyl groups are used as side chains in the calculations.

Because of their interesting optoelectronic properties and the possibility to tune their (optical) band gap through a proper design of their length, width, and edge structure, GNRs may be used as alternative to low band gap conjugated polymers (molecules) in bulk heterojunction organic solar cells. For this purpose, however, GNRs should fulfill two necessary requirements revolving around their one-electron energy diagram and optical response, respectively:[31−35] (i) On the one hand, suitable GNR donors should yield type II heterojunction in combination with common electron acceptors such as C_{60} or its soluble derivatives. Namely, an energy offset of a few tenths of an electronvolt between the LUMO (HOMO) levels of the donor and acceptor materials is typically needed to favor electron transfer from the photoexcited donor to the ground-state acceptor while preventing the corresponding hole transfer; in addition, the energy difference between the donor HOMO and the acceptor LUMO should be as large as possible to maximize the open circuit voltage (V_{oc}).[33] (ii) As light harvesting occurs primarily on the donor material in C_{60}-based organic solar cells, the GNRs should also feature strong optical absorption over the broad spectral range of the solar emission. In addition, the primary step in the dissociation process involves a Coulombically bound charge-transfer state.[36] It is believed that local electric fields at the interface, as, for example, induced by interfacial dipoles associated with electronic polarization or charge-transfer effects, can potentially reduce the barrier height for full charge separation.[37,38] Thus, the electronic structure at GNR−acceptor interfaces is also key for efficient charge photogeneration. Last but not least, low-lying triplet excited states might act as sinks for the photogenerated electron−hole pairs, which appears as an efficient competitive process in high V_{oc} material combinations, hence the need for donors with low singlet−triplet exchange energy.[39]

Here, we use first principle theoretical methods based on (time-dependent) density functional theory,

(TD)-DFT, to address the potential of A-NRs and Z-NRs with tailored width and edge topology as donors in photovoltaic cells. One should keep in mind that, in addition to the electro-optical characteristics described above, morphological issues and the optimization of device architecture are also critically important for high quantum yield solar cells.[40] Among others, these ribbons need to be properly substituted with long and possibly branched alkyl chains to be soluble in organic solvents and have good film-forming properties. Being important issues, these are, however, beyond the scope of this paper where we address the potential of GNRs in organic photovoltaics (OPV) from a theoretical point of view.

RESULTS AND DISCUSSION

The graphene nanoribbons investigated differ by their shapes and widths. The ANR_n series is built using the same monomer but with different connectivity, *para* for *p*-ANR_n and *meta* for *m*-ANR_n. The cove-shaped GNRs (CNR_n) feature cove-type edge structure and increasing width in the sequence 4-CNR_n < 6-CNR_n < 8-CNR_n. Some of these nanoribbons have been synthesized, and details about their synthesis and characterization are reported elsewhere.[41] We have performed DFT/HSE calculations of the electronic energy levels for all NRs in Figure 1 and tight-binding analysis for the two ANR series. These have been complemented for selected ribbons by DFT calculations using a long-range corrected functional, namely, wB97XD,[52] to check the robustness of the theoretical findings. The shape of the frontier molecular orbitals for all NRs studied together with a comparison between HSE and wB97XD results is given in Supporting Information. The HOMO−LUMO gaps calculated at the HSE levels are reported in Table 1 and are compared in Figure 2 to results obtained from a simple tight-binding model (where the resonance integral has been set to −3.3 eV).[42] Figure 2 shows that the HOMO−LUMO gap decreases strongly with the longitudinal size of the NRs, that is, the number *n* of repeating units. Good agreement is found between the HSE and tight-binding calculations, with the latter easily amenable to larger size ribbons and showing a saturation of the gap for a length of $n \sim 15$ units. The larger width of *m*-ANR_n compared to *p*-ANR_n translates into a smaller band gap: 1.08 eV in the polymer limit for *m*-ANR_n *versus* 1.35 eV for *p*-ANR_n.

As described before, the band gap of graphene nanoribbons is closely related to their widths, more specifically to the number *N* of carbon rows across the nanoribbon.[21] In particular, A-NRs are strictly metallic in the tight-binding approximation when the width fulfills $N = 3p + 1$ or $N = 3p + 2$ (*N* is the number of armchair chains and *p* is an integer). This is somewhat relaxed, and a small band gap opens when considering edge effect and including hydrogen passivation in density functional theory (DFT) calculations. On the other hand, A-NRs with $N = 3p$ always feature a significant band gap.[21,22] The results reported here for the two periodic structures indicate that they are both semiconductors. Note that this is consistent with the *p*-ANR_n series investigated belonging to the 3*p* family, with $N = 9$ ($p = 3$). For the sake of comparison, we have calculated the electronic structure of the 9-ANR_n nanoribbon. The DFT/HSE calculations lead to a significant lowering of the band gap when going from *p*-ANR_n (1.35 eV) to 9-ANR_n (1.09 eV). This difference emphasizes the sensitivity of the band energy diagram on the topology of the nanoribbon edges (Figure 3a).

The 4-CNR_n, 6-CNR_n, and 8-CNR_n ribbons are essentially benzo-fused zigzag nanoribbons. According to the literature, zigzag GNRs should be metallic with a zero band gap energy. Our DFT calculations indicate that the three CNRs investigated here are in fact semiconducting with a band gap between 1 and 2 eV depending on the width (Figure 3b and Table 1). To understand this apparent discrepancy, we have performed additional calculations on infinite nanoribbons where the rings at the edges are removed and substituted with H atoms (these are labeled 4-ZNR_n, 6-ZNR_n, and 8-ZNR_n). The electronic band structure of the three modified ribbons, displayed in Figure 4, is consistent with previous theoretical studies: as reported by Louie and co-workers,[22] zigzag GNRs are

TABLE 1. HOMO−LUMO Energy Gaps Calculated for the ANR_n and CNR_n Series, from Monomers to Tetramers, Together with the Polymer Band Gaps

HSE functional	monomer	dimer	trimer	tetramer	polymer
ΔE_{L-H} *p*-ANR_n (eV)	2.09	1.79	1.63	1.54	1.34
ΔE_{L-H} *m*-ANR_n (eV)	2.09	1.64	1.43	1.31	1.08
ΔE_{L-H} 4-CNR_n (eV)	3.36			2.31	2.04
ΔE_{L-H} 6-CNR_n (eV)	2.80			1.85	1.50
ΔE_{L-H} 8-CNR_n (eV)	2.48			1.53	1.18

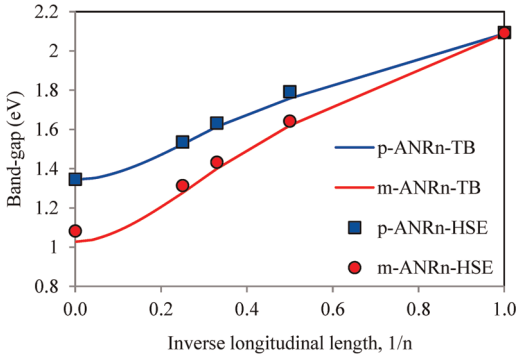

Figure 2. HOMO−LUMO energy gaps calculated for *p*-ANR_n and *m*-ANR_n at the DFT/HSE level (symbols) and TB level (solid lines), as a function of the inverse number of repeating units (0 for the infinite, periodic, structure).

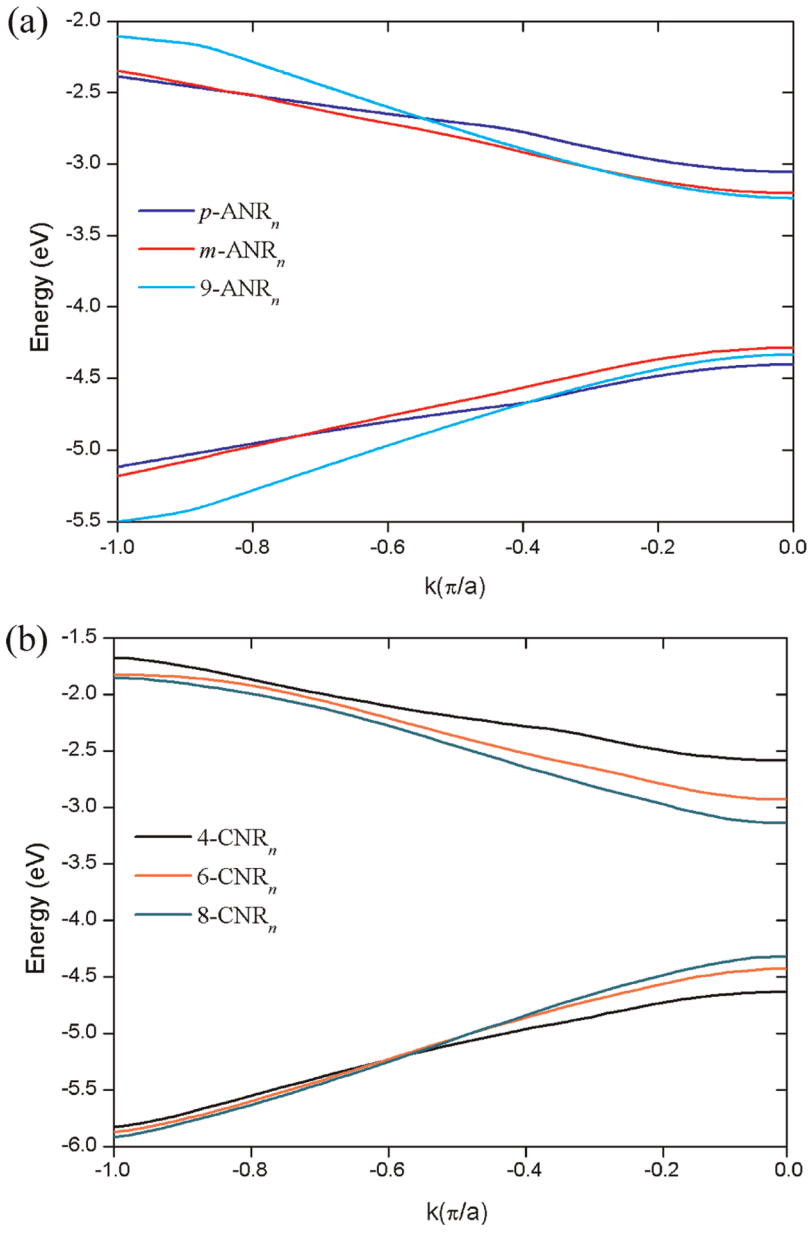

Figure 3. Band structure (half Brillouin zone) along the longitudinal axis of ANR_n (a) and CNR_n (b) series, as computed at the DFT/HSE level (*a* is the lattice constant).

characterized by a direct band gap Δ_0 (namely, the minimum difference in energy between the valence and the conductance bands) and the energy splitting Δ_1 present at the end of the Brillouin zone, where $k = 0$ (Γ point). From Figure 4, the ZNR_n series shows a vanishingly small direct band gap located at the two-third of the Brillouin zone and flat bands close to the Fermi energy, while the energy splitting at $k = 0$ decreases continuously with increasing width of the NRs. This behavior is due to the confinement of the frontier band states close to the edges of the ribbon. Comparing Figures 3b and 4, we can thus conclude that the sole presence of the benzo-fused edge groups in the CNR_n series breaks the electronic confinement of the wave function close to the Fermi energy and is responsible for the opening of a band gap.

Since all of the GNRs investigated here feature a finite band gap, it is of interest to assess their potential as electron donors in the fabrication of OPV cells. As described earlier, a first requirement deals with the one-electron energy structure, which should favor the formation of thermodynamically stable charge-separated states from the lowest excited state of the donor. For the sake of comparison, we have also calculated at the same level of theory the electronic band structure of poly(3-hexylthiophene) (P3HT), a work horse for polymer donors used in bulk heterojunction (BHJ) solar cells, and the frontier energy levels of C_{60}, used as acceptor (or rather its soluble version phenyl-C_{61}-butyric acid methyl ester, PCBM) in combination with conjugated polymers in prototypical BHJ devices. As

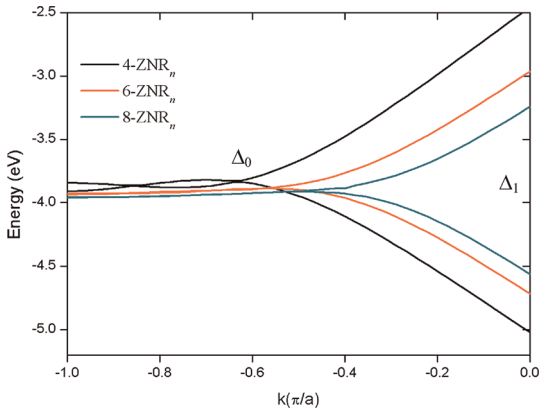

Figure 4. Band structure (half Brillouin zone) along the longitudinal axis of the zigzag NRs. Δ_0 is referred to as the direct bang gap, while Δ_1 is the energy splitting at the end of the Brillouin zone (k = 0 or Γ point).

TABLE 2. Valence Band (VB) Energy, Conduction Band (CB) Energy, and Band Gap Value for GNRs and P3HT Polymer[a]

	p-ANR$_n$	*m*-ANR$_n$	4-CNR$_n$	6-CNR$_n$	8-CNR$_n$	P3HT$_n$	C$_{60}$
VB (eV)	−4.40	−4.28	−4.63	−4.43	−4.32	−4.19	−5.95
CB (eV)	−3.06	−3.20	−2.59	−2.93	−3.14	−2.55	−3.62
band gap (eV)	1.34	1.08	2.04	1.50	1.18	1.64	2.33
ΔE LUMO$_{(A-D)}$	0.56	0.42	1.03	0.69	0.48	1.07	

[a] HOMO and LUMO energies and HOMO−LUMO gap are also given for C$_{60}$. The energy mismatch between the donor (GNRs and P3HT) and the acceptor (C$_{60}$ molecule) LUMO levels is also reported.

reported in the literature,[43] the "anti" configuration of the P3HT backbone is the most stable, with a shallow minimum corresponding to an equilibrium torsion angle between successive rings in the gas phase of about 150°. However, the conjunction of packing forces in the solid together with van der Waals interactions between the alkyl side chains drives the conformation of P3HT chains into a close to planar structure,[44] which has therefore been adopted in our electronic structure calculations. In addition, to save computational efforts, the long alkyl side chains have been substituted with methyl groups, which should not affect the electronic and optical properties of isolated chains. The energy values of the valence and conduction band edges for the graphene nanoribbons and P3HT are listed in Table 2 and plotted in Figure 5, together with the HOMO and LUMO energies of C$_{60}$.

From both Figure 5 and Table 2, it is clear that all GNRs investigated here have a lower electron affinity than C$_{60}$ and give rise to an energy mismatch between the donor and acceptor LUMO levels larger than 0.4 eV at the HSE level (0.42 and 0.48 eV for *m*-ANR$_n$ and 8-CNR$_n$, respectively; for all other NRs studied, this value is higher than 0.5 eV). Qualitatively, this energy difference is on the order of the typical exciton binding energy in organic materials[46] and should thus provide the necessary driving force for splitting the excitons

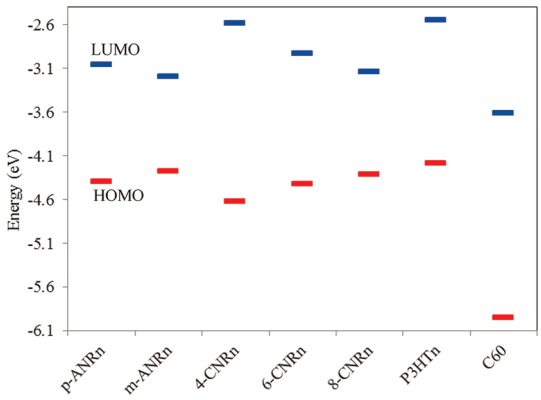

Figure 5. One-electron energy diagram for GNRs, P3HT (donors), and C$_{60}$ (acceptor).

into free charge carriers at GNR/C$_{60}$ interfaces. Yet, we stress that the HSE functional is known to underestimate the quasiparticle gap, in comparison to the more reliable GW appoach,[45] thus a quantitative assessment from the HSE results should be considered with care. We further note that the *relative* positioning of the energy levels should be accurately described at the HSE level. As a matter of fact, the HSE results yield a driving force of about 1 eV for the P3HT/C$_{60}$ interface, which is in very good agreement with experiment.[47] In addition, the valence band edge of the graphene nanoribbons is shifted down in energy compared to P3HT by up to 0.4 eV. As the open circuit voltage is, in the simplest picture, related to the energy difference between the donor HOMO and the acceptor LUMO, this should translate into higher V_{oc} and therefore higher power conversion yield in solar cells where GNRs substitute P3HT.

Polymer donors in organic photovoltaic cells are primarily used to harvest sunlight. There is abundant recent literature on the design and synthesis of low band gap conjugated (co)polymers and their use as donors in organic solar cells.[31,35,48,49] Clearly, if GNRs are to be used for this purpose, they need to exhibit, in addition to the proper energy alignment with acceptors discussed above, strong absorption in the visible and infrared spectral range. For the simulation of the optical properties, we resort to finite oligomers (as the TD-DFT approach implemented in Gaussian09 cannot be applied to periodic systems). Moreover, the nanoribbons synthesized by the bottom-up approach (namely, *m*-ANR$_n$) display a broad distribution in physical lengths, which is indicated by a polydispersity index (PDI) of 1.1−2.2, as measured by analytical gel permeation chromatography (GPC). We have thus analyzed the evolution of the absorption spectra with the longitudinal size (from n = 1 to n = 4) of the nanoribbons; see Supporting Information. These show profound changes in the number and relative intensity of the main absorption bands from n = 1 to n = 3, while the overall shape of the spectra remains unchanged

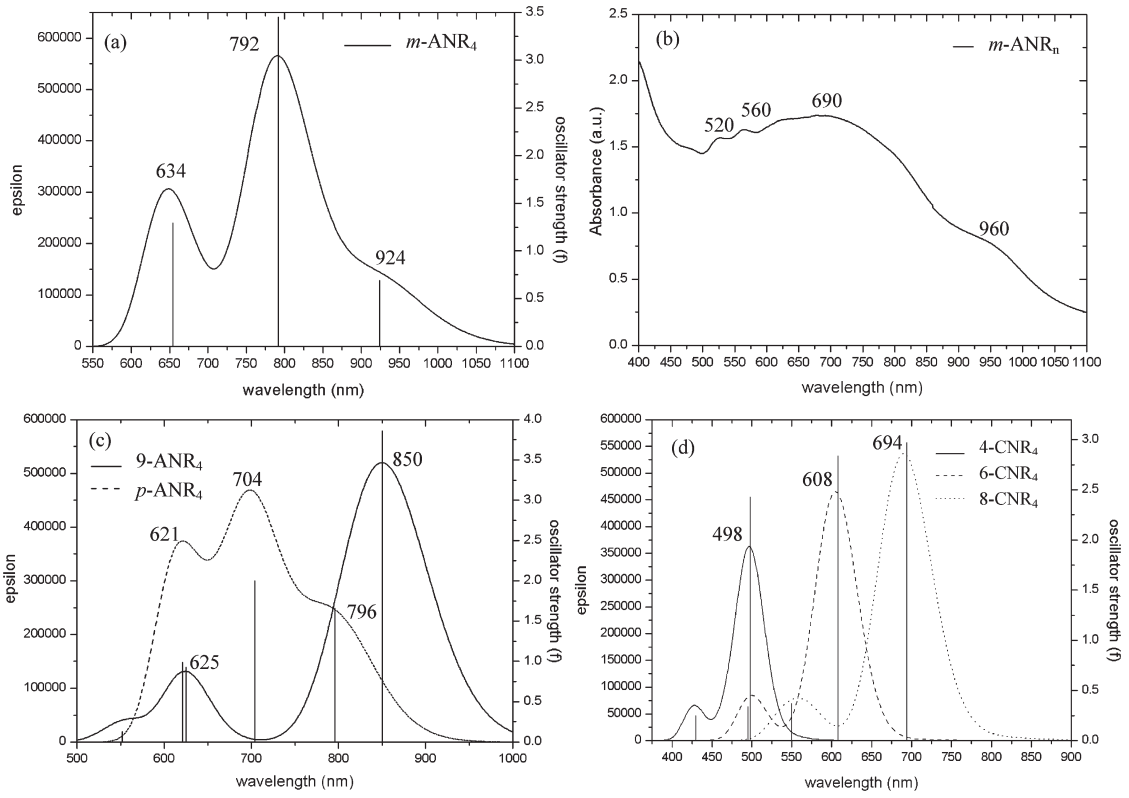

Figure 6. Simulated absorption spectra for *m*-ANR$_4$ (a); *p*-ANR$_4$ (dash line) and 9-ANR$_4$ (c); 4-CNR$_4$, 6-CNR$_4$, and 8-CNR$_4$ in solid, dashed, and dotted lines, respectively (d). Experimental absorption spectrum for *m*-ANR$_n$ (b). The vertical lines in the simulated spectra indicate the oscillator strengths.

when going to longer ribbons (except, of course, for the red shift of all absorption peaks consistent with the increased delocalization size expected from a particle in the box picture).

The optical absorption spectrum computed for the *m*-ANR$_4$ (Figure 6a) is in good agreement with that measured for the corresponding nanoribbon in *N*-methyl-2-pyrrolidone (Figure 6b): the experimental spectrum features a strong and broad band in the range of 500−800 nm with a shoulder at ∼960 nm, which compares favorably to the computed spectrum with two intense bands at 634 and 792 nm and a shoulder at 923 nm. As found for *m*-ANR$_4$, the absorption spectrum predicted for *p*-ANR$_4$ (Figure 6c) shows two main bands in the visible with a shoulder at low energy (yet the full spectrum of *m*-ANR$_4$ is red-shifted with respect to *p*-ANR$_4$, as expected from the difference in the width of the two nanoribbons). In contrast to the armchair ribbons that feature a rich structure with multiple peaks and shoulders, the calculated absorption spectra of the cove-shaped ribbons are dominated by a single peak at 498 nm in 4-CNR$_4$, 608 nm in 6-CNR$_4$, and 694 nm in 8-CNR$_4$ (Figure 6d).

To assess the role of edge effects on the shape of the absorption spectrum, we have applied the same TD-DFT methodology to describe the excited states of nanoribbon 9-ANR$_4$ lacking the benzo-fused rings at the lateral edges. In line with the small (0.16 eV) lowering of the band gap in 9-ANR$_4$ compared to *p*-ANR$_4$, the lowest optical transition is red-shifted (by 0.1 eV) when going from the latter to the former (Figure 6c). As a matter of fact, the lowest excited state in both ribbons is dominated by a HOMO−LUMO electronic excitation. As can be clearly seen in Figure 6c, the presence of the edge units has a more profound impact on the shape of the absorption spectrum and is responsible for the presence of multiple bands in the visible range. Through a detailed analysis of the excited-state wave functions, it turns out that the second optical transition in 9-ANR$_4$ (at ∼625 nm) corresponds to the third weak band in *p*-ANR$_4$ (at ∼621 nm). The main difference between the two spectra lies in the presence of an additional, strongly allowed, optical excitation on the *p*-ANR$_4$ spectrum (at ∼704 nm), which is associated with the extension of the π-system along the lateral direction. Thus, though *p*-ANR$_4$ is essentially an armchair graphene nanoribbon featuring nine carbon rows as 9-ANR$_4$, edge effects brought about by the bottom-up synthesis of the armchair ribbons studied here give rise to a more complex absorption spectrum with additional strong absorption bands in the visible.

Focusing on the CNR$_n$ series, the TD-DFT calculations show the expected continuous bathochromic shift upon increasing the width of the nanoribbons (Figure 6d). In all cases, the lowest excited state

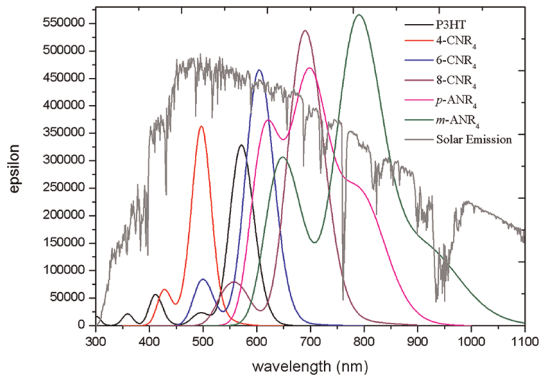

Figure 7. Overlap of calculated absorption spectra of GNRs with the solar emission spectrum (incident optical power density under standard conditions: air mass 1.5 global sunlight, 100 mW cm^{-2} at 298 K). The P3HT spectrum is calculated for an octamer, while the NRs' spectra are for tetramers.

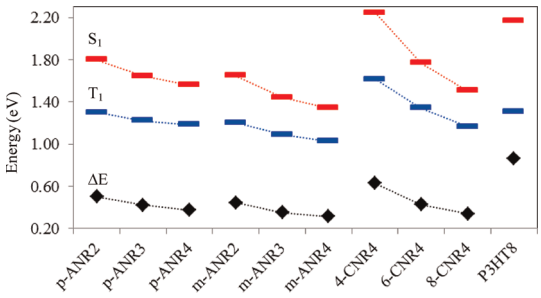

Figure 8. Transition energies from the singlet ground state to the lowest singlet (S_1) and triplet (T_1) excited states and S_1-T_1 energy gap for all of the NRs studied. The dotted lines are a guide to the eye.

primarily involves a HOMO−LUMO transition. As described above, the most striking result for the CNR$_n$ series is the fact that these display a semiconductor behavior with strong absorption of light in the visible range, which differs significantly from the photophysical behavior of perfectly zigzag nanoribbons with zero band gap. Once again, this points to the large impact of the edge effects on the electronic and optical properties of GNRs.

It is worth looking more closely at these results in the light of their potential application as antennas in organic solar cells. From the comparison of the simulated absorption spectra of the studied GNRs and the reference conjugated polymer (the 8-unit P3HT$_8$ chain) in Figure 7, one can clearly see that the GNRs strongly absorb light across the visible and infrared spectral regions, which should translate into efficient harvesting of the solar emission. It is indeed commonly admitted in the low band gap polymer community that developing materials with a broad absorption band down to 1.5−1.2 eV and a high extinction coefficient (of at least 10^5 cm^{-1}) is a prerequisite for higher photoconversion efficiencies. In that respect, the armchair GNRs seem particularly appealing as these display stronger absorption than P3HT$_8$ in a broader and red-shifted region of the spectrum that matches closely with the solar emission.

Finally, we would like to address two additional issues in a number of organic-based solar cells. The first one deals with the possibility that low-lying donor triplet excited states act as sinks in the charge generation process. This will be particularly important in high V_{oc} material combinations where large exchange interactions can bring the lowest triplet exciton, T_1, below the charge-transfer state.[39] It is thus instructive to see how the S_1-T_1 energy gap compares to conjugated polymers, namely, to P3HT. In Figure 8, we report the vertical excitation energies from the S_0 ground state to both the S_1 and T_1 excited states, as well as their energy difference for the two series of NRs investigated and the 8-unit P3HT$_8$ chain. These have been obtained at the TD-DFT level, as unrestricted DFT calculations tend to underestimate the S_0-T_1 energy gap;[50] see Supporting Information. As found for conjugated polymers, the energy of the S_0-S_1 transition decreases faster with increasing ribbon longitudinal size than that of the S_0-T_1 transition, leading to a reduction of the S_1-T_1 energy gap. This reflects the more localized character of the T_1 excited-state wave function.[51] Yet, we find that the S_1-T_1 exchange energy converges to a value (of about 0.3 eV) that is considerably smaller than the corresponding quantity in P3HT$_8$ (∼0.9 eV), suggesting an increased electron−hole radius of the lowest electronic excitations in the ribbons. We note in passing that the singlet−triplet energy gap computed at the TD-DFT/HSE level for P3HT is close to that reported from phosphorescence measurements on a number of rigid-rod conjugated polymers (on the order of 0.7 eV).[51]

A second issue concerns the one-electron energy picture of Figure 5. Though this is still open to debate, it seems that the driving force for charge separation brought by the energy level offset between donor and acceptor in polymer BHJ cells might be at least partly lost as heat during fast thermalization of the initially hot charge-transfer (CT) states. This then raises the question of the mechanisms responsible for the splitting of the resulting fully relaxed Coulomb bound electron−hole pairs. In that respect, a substantial reshuffling of the electronic density has been demonstrated at organic interfaces that can either favor or impede splitting of the CT states.[37,38]

To address this question, we have modeled at the DFT level a simple donor−acceptor complex comprising one *p*-ANR$_2$ nanoribbon interacting with a C_{60} molecule, as well as the P3HT$_8$/C_{60} pair for comparison. The geometric structure of both systems has been fully relaxed accounting for dispersion interactions using the wB97XD DFT functional,[52] and a single-point calculation has been performed at the HSE level on the basis of this equilibrium geometry. In line with the energy diagram of Figure 5, the HOMO of the complex is essentially confined on the GNR donor while the

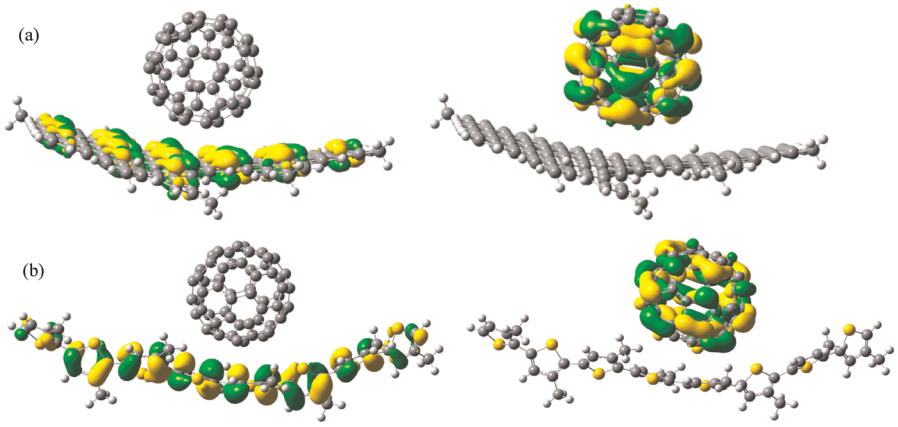

Figure 9. (a) HOMO (left) and LUMO (right) orbitals at the *p*-ANR$_2$/C$_{60}$ interface. (b) HOMO (left) and LUMO (right) orbitals at the P3HT$_8$/C$_{60}$ interface.

LUMO is on the fullerene acceptor (Figure 9a). Yet, by comparison to the energy values computed for the isolated molecules, the C_{60} LUMO level is shifted up in energy (destabilized) by about 0.46 eV while the *p*-ANR_2 HOMO is shifted down by 0.06 eV. This arises because of a conjunction of electrostatic effects (more precisely, the unbalanced quadrupolar field at the interface) and partial charge transfer (by about 0.10 |e|) in the electronic ground state.[37,38] For the P3HT/fullerene interface investigated here, a similar behavior is predicted, with the same localization of the frontier orbitals in the complex (HOMO confined on the donor and LUMO on the acceptor, Figure 9b). In this case, the C_{60} LUMO level is shifted up by about 0.16 eV while the $P3HT_8$ HOMO is stabilized by 0.43 eV. Once again, this arises because of electrostatic effects and partial ground-state charge transfer (by about 0.20 |e|). Thus, the DFT calculations suggest that electrons and holes close to the interface experience a local electric field that tends to expel them into the bulk. Interestingly, the magnitude of this effect on the order of half an electronvolt is commensurate with the CT binding energy[53,54] and should thus promote the formation of free charge carriers.

CONCLUSIONS

In summary, the electronic and optical properties of novel GNR structures have been modeled using DFT and TD-DFT methods. We found that the width of the ribbons together with their topology and edge structures dictate their electronic band structure and optical absorption spectra. In the ANR_n series, the broader width of *m*-ANR_n compared to *p*-ANR_n translates into a smaller band gap (1.08 *vs* 1.35 eV), while for the CNR_n series the sole presence of benzo-fused edge groups is responsible for the opening up of a band gap to reach values between 1.2 and 2.0 eV. The optical absorption spectra of the ANR_n ribbons show two main bands in the visible with a shoulder at low energy (and red-shifted bands for *m*-ANR_n with respect to *p*-ANR_n), while the CNR_n ribbons display a semiconductor behavior with strong absorption of light in the visible range, in contrast to zigzag nanoribbons with zero band gap. All GNRs studied have a lower electron affinity than C_{60}, with energy mismatch between the LUMO levels as large as 0.4 eV and valence band edge shifted up in energy compared to P3HT by up to 0.4 eV. In addition, they strongly absorb light across the visible and infrared spectral regions that should translate into efficient harvesting of the solar emission. Likely because of electron delocalization along the lateral direction, the S_1-T_1 energy gap of about 0.3 eV is much smaller than that encountered in conjugated polymers, which should reduce the triplet losses in high V_{oc} solar cells. Finally, rearrangement of the electronic density at GNR/C_{60} interfaces strongly perturbs the energy diagram for electrons and holes favoring the splitting of the CT pairs into free charge carriers. Altogether, the electronic and optical properties of GNRs seem to be particularly well-suited to ensure sunlight absorption and photoconversion at interfaces with fullerenes in OPV devices. Work along that direction is currently in progress.

METHODS

DFT calculations were performed on NRs of finite longitudinal lengths as well as for the corresponding infinite nanoribbons using periodic boundary conditions (see Figure 1 for chemical structures). A k-point sampling of 27 (47) k points that are uniformly positioned along the 1D Brillouin zone is employed for ANR_n (CNR_n) series, with armchair (cove)-shaped edges (*n* denotes the number of repeating units or monomers). The screened exchange hybrid density functional HSE,[55] which has been shown to accurately reproduce experimental band gaps of molecules and solids,[56,57] has been used. For instance, HSE calculations yield a HOMO–LUMO gap of 2.09 eV in the monomer ANR_1, in excellent agreement with the ~2.1 eV experimental value.[58] An electrostatic potential (ESP) charge analysis

has been carried out for the interface between *p*-ANR_2 and the C_{60} molecule. All reported electronic properties are given for fully optimized geometric structures using the polarized 6-31G* Gaussian basis set.[59] TD-DFT calculations were performed to assess the electronic singlet and triplet excited states of finite NRs and to simulate their optical absorption spectra, using the same screened exchange hybrid density functional and the 6-31G* basis set. All of the calculations presented in this work were performed using the development version of the GAUSSIAN09 suite of programs.[60] Finally, tight-binding calculations[42] were also performed to address the convergence of the band gap with *n*. Optical absorption spectrum was measured at room temperature on a Perkin-Elmer Lambda 100 spectrophotometer in *N*-methyl-2-pyrrolidone (NMP). The GNR sample (0.5 mg) was dispersed in NMP (5.0 mL) by sonication for 30 min and subjected to centrifugation (1000 rpm, 40 min). The supernatant solution (3.0 mL) was taken and used for the absorption measurement.[41]

Conflict of Interest: The authors declare no competing financial interest.

Acknowledgment. This work is supported by the European Commission Seventh Framework Program (FP7/2007-2013) under grant agreement number 228424 (Project MINOTOR) and 238177 (Project ITN-SUPERIOR) and by the Belgian National Fund for Scientific Research (FNRS). D.B. is a FNRS Research Director.

Supporting Information Available: Molecular orbital shapes, absorption spectra plots of all NRs investigated, comparison with the long-range wB97XD functional, U-DFT triplet analysis, relaxed S_1 geometry for the $n = 1$ ribbon and optimized geometrical structures of the $n = 4$ ribbons and the *p*-ANR_2/C_{60} interface. This material is available free of charge *via* the Internet at http://pubs.acs.org.

REFERENCES AND NOTES

1. Boehm, H. P. Graphene—How a Laboratory Curiosity Suddenly Became Extremely Interesting. *Angew. Chem., Int. Ed.* **2010**, *49*, 9332–9335.
2. Novoselov, K. S.; Geim, A. K.; Morozov, S. V.; Jiang, D.; Zhang, Y.; Dubonos, S. V.; Grigorieva, I. V.; Firsov, A. A. Electric Field Effect in Atomically Thin Carbon Films. *Science* **2004**, *306*, 666.
3. Berger, C.; Song, Z.; Li, T.; Li, X.; Ogbazghi, A. Y.; Feng, R.; Dai, Z.; Marchenkov, A. N.; Conrad, E. H.; First, P. N.; *et al.* Ultrathin Epitaxial Graphite: 2D Electron Gas Properties and a Route toward Graphene-Based Nanoelectronics. *J. Phys. Chem. B* **2004**, *108*, 19912–19916.
4. Geim, A. K.; Novoselov, K. S. The Rise of Graphene. *Nat. Mater.* **2007**, *6*, 183–191.
5. Geim, A. K. Graphene: Status and Prospects. *Science* **2009**, *324*, 1530–1534.
6. Zhu, Y.; Murali, S.; Cai, W.; Li, X.; Suk, J. W.; Potts, J. R.; Ruoff, R. S. Graphene and Graphene Oxide: Synthesis, Properties, and Applications. *Adv. Mater.* **2010**, *22*, 3906–3924.
7. Son, Y.-W; Cohen, L. M.; Louie, G. S. Half-Metallic Graphene Nanoribbons. *Nature* **2006**, *444*, 347.
8. Wakabayashi, K. Electronic Transport Properties of Nanographite Ribbon Junctions. *Phys. Rev. B* **2001**, *64*, 125428.
9. Barone, V.; Hod, O.; Scuseria, G. E. Electronic Structure and Stability of Semiconducting Graphene Nanoribbons. *Nano Lett.* **2006**, *6*, 2748–2754.
10. Areshkin, D. A.; Gunlycke, D.; White, C. T. Ballistic Transport in Graphene Nanostrips in the Presence of Disorder: Importance of Edge Effects. *Nano Lett.* **2007**, *7*, 204–210.
11. Ezawa, M. Peculiar Width Dependence of the Electronic Properties of Carbon Nanoribbons. *Phys. Rev. B* **2006**, *73*, 045432.
12. Kaway, T.; Miyamoto, Y.; Sugino, O.; Koga, Y. Graphitic Ribbons without Hydrogen-Termination: Electronic Structures and Stabilities. *Phys. Rev. B* **2000**, *62*, R16349–R16352.
13. Han, M. Y.; Özyilmaz, B.; Zhang, Y.; Kim, P. Energy Bandgap Engineering of Graphene Nanoribbons. *Phys. Rev. Lett.* **2007**, *98*, 206805.
14. Chen, Z.; Lin, Y. M.; Rooks, M. J.; Avouris, P. Graphene Nano-Ribbon Electronics. *Phys. E* **2007**, *40*, 228–232.
15. Fujita, M.; Wakabayashi, K.; Nakada, K.; Kusakabe, K. Peculiar Localized State at Zigzag Graphite Edge. *J. Phys. Soc. Jpn.* **1996**, *65*, 1920–1923.
16. Nakada, K.; Fujita, M.; Dresselhaus, G.; Dresselhaus, M. S. Edge State in Graphene Ribbons: Nanometer Size Effect and Edge Shape Dependence. *Phys. Rev. B* **1996**, *54*, 17954–17961.
17. Wakabayashi, K.; Fujita, M.; Ajiki, H.; Sigrist, M. Electronic and Magnetic Properties of Nanographite Ribbons. *Phys. Rev. B* **1999**, *59*, 8271–8282.
18. Brey, L.; Fertig, H. A. Electronic States of Graphene Nanoribbons Studied with the Dirac Equation. *Phys. Rev. B* **2006**, *73*, 235411.
19. Raza, H. Edge and Passivation Effects in Armchair Graphene Nanoribbons. *Phys. Rev. B* **2011**, *84*, 165425.
20. Bai, J.; Huang, Y. Fabrication and Electrical Properties of Graphene Nanoribbons. *Mater. Sci. Eng.* **2010**, *R70*, 341–353.
21. Son, Y.-W.; Cohen, M. L.; Louie, S. G. Energy Gaps in Graphene Nanoribbons. *Phys. Rev. Lett.* **2006**, *97*, 216803.
22. Yang, L.; Park, C. H.; Son, Y. W.; Cohen, M. L.; Louie, S. G. Quasiparticle Energies and Band Gaps in Graphene Nanoribbons. *Phys. Rev. Lett.* **2007**, *99*, 186801.
23. Okada, S.; Oshiyama, A. Magnetic Ordering in Hexagonally Bonded Sheets with First-Row Elements. *Phys. Rev. Lett.* **2001**, *87*, 146803.
24. Lee, H.; Son, Y. W.; Park, N.; Han, S.; Yu, J. Magnetic Ordering at the Edges of Graphitic Fragments: Magnetic Tail Interactions between the Edge-Localized States. *Phys. Rev. B* **2005**, *72*, 174431.
25. Raza, H. Zigzag Graphene Nanoribbons: Bandgap and Midgap State Modulation. *J. Phys.: Condens. Matter* **2011**, *23*, 382203.
26. Hsu, H.; Reichl, L. E. Selection Rule for the Optical Absorption of Graphene Nanoribbons. *Phys. Rev. B* **2007**, *76*, 045418.
27. Prezzi, D.; Varsano, D.; Ruini, A.; Molinari, E. Quantum Dot States and Optical Excitations of Edge-Modulated Graphene Nanoribbons. *Phys. Rev. B* **2011**, *84*, 041401.
28. Gundra, K.; Shukla, A. Theory of the Electro-Optical Properties of Graphene Nanoribbons. *Phys. Rev. B* **2011**, *83*, 075413.
29. Yang, L.; Cohen, M. L.; Louie, S. G. Excitonic Effects in the Optical Spectra of Graphene Nanoribbons. *Nano Lett.* **2007**, *7*, 3112–3115.
30. Sasaki, K.; Kato, K.; Tokura, Y.; Oguri, K.; Sogawa, T. Theory of Optical Transitions in Graphene Nanoribbons. *Phys. Rev. B* **2011**, *84*, 085458.
31. Thompson, B. C.; Fréchet, J. M. J. Polymer−Fullerene Composite Solar Cells. *Angew. Chem., Int. Ed.* **2008**, *47*, 58–77.
32. Forrest, S. R. The Limits to Organic Photovoltaic Cell Efficiency. *MRS Bull.* **2005**, *30*, 28–32.
33. Scharber, M. C.; Mühlbacher, D.; Koppe, M.; Denk, P.; Waldauf, C.; Heeger, A. J.; Brabec, C. J. Design Rules for Donors in Bulk-Heterojunction Solar Cells: Toward 10% Energy Convertion Efficiency. *Adv. Mater.* **2006**, *18*, 789–794.
34. Xue, J.; Rand, B. P.; Uchida, S.; Forrest, S. R. A Hybrid Planar-Mixed Molecular Heterojunction Photovoltaic Cell. *Adv. Mater.* **2005**, *17*, 66.
35. Yang, F.; Shtein, M.; Forrest, S. R. Controlled Growth of a Molecular Bulk Heterojunction Photovoltaic Cell. *Nat. Mater.* **2005**, *4*, 37–41.
36. Brédas, J. L.; Norton, J. S.; Cornil, J.; Coropceanu, V. Molecular Understanding of Organic Solar Cells: The Challenges. *Acc. Chem. Res.* **2009**, *42*, 1691–1699.
37. Beljonne, D.; Cornil, J.; Castet, F.; Muccioli, L.; Zannoni, C.; Brédas, J. L. Electronic Processes at Organic−Organic Interfaces: Insight from Modeling and Implications for Opto-Electronic Devices. *Chem. Mater.* **2011**, *23*, 591–609.
38. Verlaak, S.; Beljonne, D.; Cheyns, D.; Rolin, C.; Linares, M.; Castet, F.; Cornil, J.; Heremans, P. Electronic Structure and

Geminate Pair Energetics at Organic–Organic Interfaces: The Case of Pentacene/C_{60} Heterojunctions. *Adv. Funct. Mater.* **2009**, *19*, 3809–3814.
39. Westenhoff, S.; Howard, I. A.; Hodgkiss, J. M.; Kirov, K. R.; Bronstein, H. A.; Williams, C. K.; Greenham, N. C.; Friend, R. H. Charge Recombination in Organic Photovoltaic Devices with High Open-Circuit Voltage. *J. Am. Chem. Soc.* **2008**, *130*, 13653–13658.
40. Liu, J.; Shi, Y.; Yang, Y. Solvation-Induced Morphology Effects on the Performance of Polymer-Based Photovoltaic Devices. *Adv. Funct. Mater.* **2001**, *11*, 420–421.
41. Schwab, M. G.; Narita, A.; Hernandez, Y.; Mali, K.; de Feyter, S.; Feng, X.; Müllen, K. Structurally Well-Defined Graphene Nanoribbons of Exceptional Width and Length. Submitted for publication.
42. Reich, S.; Maultzsch, J.; Thomsen, C.; Ordejòn, P. Tight-Binding Description of Graphene. *Phys. Rev. B* **2002**, *66*, 035412.
43. Pizzirusso, A.; Savini, M.; Muccioli, L.; Zannoni, C. An Atomistic Simulation of the Liquid-Crystalline Phases of Sexithiophene. *J. Mater. Chem.* **2011**, *21*, 125–133.
44. Mena-Osteritz, E.; Meyer, A.; Langeveld-Voss, B. M. W.; Janssen, R. A. J.; Meijer, E. W.; Bauerle, P. Two-Dimensional Crystal of Poly(3-alkyl-thiophene)s: Direct Visualization of Polymer Folds in Submolecular Resolution. *Angew. Chem., Int. Ed.* **2000**, *39*, 2679–2684.
45. Jain, M.; Chelikowsky, J. R.; Louie, S. G. Reliability of Hybrid Functionals in Predicting Band Gaps. *Phys. Rev. Lett.* **2011**, *107*, 216806.
46. Bakulin, A. A.; Rao, A.; Pavelyev, V. G.; van Loosdrecht, P. H. M.; Pshenichnikov, M. S.; Niedzialek, D.; Cornil, J.; Beljonne, D.; Friend, R. H. The Role of Driving Energy and Delocalized States for Charge Separation in Organic Semiconductors. *Science* **2012**, *335*, 1340–1344.
47. Rait, S.; Kashyap, S.; Bhatnagar, P. K.; Mathur, P. C.; Sengupta, S. K.; Kumar, J. Improving Power Conversion Efficiency in Polythiophene/Fullerene-Based Bulk Heterojunction Solar Cells. *Sol. Energy Mater. Sol. Cells* **2007**, *91*, 757–763.
48. Carlé, J. E.; Andreasen, J. W.; Jørgensen, M.; Krebs, F. C. Low Band Gap Polymers Based on 1,4-Dialkoxybenzene, Thiophene, Bithiophene Donors and the Benzothiadiazole Acceptor. *Sol. Energy Mater. Sol. Cells* **2011**, *94*, 774–780.
49. O'Boyle, N. M.; Campbell, C. M.; Hutcison, G. R. Computational Design and Selection of Optimal Organic Photovoltaic Materials. *J. Phys. Chem. C* **2011**, *115*, 16200–162010.
50. Hajgató, B.; Szieberth, D.; Geerlings, P.; De Proft, F.; Deleuze, M. S. A Benchmark Theoretical Study of the Electronic Ground State and of the Singlet-Triplet Split of Benzene and Linear Acenes. *J. Chem. Phys.* **2009**, *131*, 224321.
51. Köhler, A.; Beljonne, D. The Singlet–Triplet Exchange Energy in Conjugated Polymers. *Adv. Funct. Mater.* **2004**, *14*, 11–18.
52. Chai, J.-D.; Head-Gordon, M. Long-Range Corrected Hybrid Density Functionals with Damped Atom–Atom Dispersion Corrections. *Phys. Chem. Chem. Phys.* **2008**, *10*, 6615–6620.
53. Ohkita, H.; Cook, S.; Astuti, Y.; Duffy, W.; Tierney, S.; Zhang, W.; Heeney, M.; McCulloch, I.; Nelson, J.; Bradley, D. D. C.; *et al.* Charge Carrier Formation in Polythiophene/Fullerene Blend Films Studied by Transient Absorption Spectroscopy. *J. Am. Chem. Soc.* **2008**, *130*, 3030–3042.
54. Shoaee, S.; Clarke, T. M.; Huang, C.; Barlow, S.; Marder, S. R.; Heeney, M.; McCulloch, I.; Durrant, J. R. Acceptor Energy Level Control of Charge Photogeneration in Organic Donor/Acceptor Blends. *J. Am. Chem. Soc.* **2010**, *132*, 12919–12926.
55. Heyd, J.; Scuseria, G. E.; Ernzerhorf, M. Hybrid Functionals Based on a Screened Coulomb Potential. *J. Chem. Phys.* **2003**, *118*, 8207.
56. Heyd, J.; Scuseria, G. E. Efficient Hybrid Density Functional Calculations in Solids: Assessment of the Heyd–Scuseria–Ernzerhof Screened Coulomb Hybrid Functional. *J. Chem. Phys.* **2004**, *121*, 1187–1192.
57. Heyd, J.; Peralta, J. E.; Scuseria, G. E. Energy Band Gaps and Lattice Parameters Evaluated with the Heyd–Scuseria–Ernzerhof Screened Hybrid Functional. *J. Chem. Phys.* **2005**, *123*, 174101.
58. Böhme, T.; Simpson, C. D.; Müllen, K.; Rabe, J. P. Current–Voltage Characteristics of a Homologous Series of Polycyclic Aromatic Hydrocarbons. *Chem.—Eur. J.* **2007**, *13*, 7349.
59. Rassolov, V. A.; Ratner, M. A.; Pople, J. A.; Redfern, P. C.; Curtiss, L. A. 6-31G* Basis Set for Third-Row Atoms. *J. Comput. Chem.* **2001**, *22*, 976–984.
60. Vreven, T.; Montgomery, J. A., Jr.; Peralta, J. E.; Ogliaro, F.; Bearpark, M.; Heyd, J. J.; Brothers, E.; Kudin, K. N.; Staroverov, V. N.; Kobayashi, R.; *et al. Gaussian 09*, revision A.1; Gaussian, Inc.: Wallingford, CT, 2009.